



1 **Different physicochemical behaviors of nitrate and ammonium**  
2 **during transport: a case study on Mt. Hua, China**

3

4 Can Wu<sup>1</sup>, Cong Cao<sup>2,a</sup>, Jianjun Li<sup>2</sup>, Shaojun Lv<sup>1</sup>, Jin Li<sup>2,b</sup>, Xiaodi Liu<sup>1</sup>, Si Zhang<sup>1</sup>,  
5 Shijie Liu<sup>1</sup>, Fan Zhang<sup>1</sup>, Jingjing Meng<sup>4</sup>, Gehui Wang<sup>1,3\*</sup>

6

7

8

9 <sup>1</sup>Key Lab of Geographic Information Science of the Ministry of Education, School of  
10 Geographic Sciences, East China Normal University, Shanghai 200062, China

11 <sup>2</sup>State Key Laboratory of Loess and Quaternary Geology, Institute of Earth  
12 Environment, Chinese Academy of Sciences, Xi'an 710061, China

13 <sup>3</sup>Institute of Eco-Chongming, Chenjia Zhen, Chongming, Shanghai 202162, China

14 <sup>4</sup>School of Environment and Planning, Liaocheng University, Liaocheng 252000,  
15 China

16

17 <sup>a</sup>Now at The State University of New York at Stony Brook.

18 <sup>b</sup>Now at Institute for Environmental and Climate Research, Jinan University.

19

20

21

22

23

24 \*Corresponding author. Gehui Wang ([ghwang@geo.ecnu.edu.cn](mailto:ghwang@geo.ecnu.edu.cn))

25

26

27

28

29

30

31

32

33

34

35



36 **Abstract:** To understand the chemical evolution of aerosols in the transport process,  
37 the chemistry of PM<sub>2.5</sub> and nitrogen isotope compositions on the mountainside of Mt.  
38 Hua (~1120 m a.s.l.) in inland China during the 2016 summertime were investigated  
39 and compared with parallel observations collected at surface sampling site (~400 m  
40 a.s.l.). PM<sub>2.5</sub> exhibited a high level at the surface (aver. 76.0±44.1 μg/m<sup>3</sup>) and could be  
41 transported aloft by anabatic valley winds, leading to the gradual accumulation of  
42 daytime PM<sub>2.5</sub> with a noon peak at the mountainside sampling site. As the predominant  
43 ion species, sulfate exhibited nearly identical mass concentrations in both sites, but its  
44 PM<sub>2.5</sub> mass fraction was moderately enhanced by ~4% at the higher elevation. The  
45 ammonium variations were similar to the sulfate variations, the chemical forms of both  
46 of which mainly existed as ammonium bisulfate (NH<sub>4</sub>HSO<sub>4</sub>) and ammonium sulfate  
47 ((NH<sub>4</sub>)<sub>2</sub>SO<sub>4</sub>) at the lower and higher elevations, respectively. Unlike sulfate and  
48 ammonium, nitrate mainly existed as ammonium nitrate (NH<sub>4</sub>NO<sub>3</sub>) in fine particles and  
49 exhibited decreasing mass concentration and proportion trends with increasing  
50 elevation. This finding was ascribed to NH<sub>4</sub>NO<sub>3</sub> volatilization, in which gaseous HNO<sub>3</sub>  
51 from semi-volatile NH<sub>4</sub>NO<sub>3</sub> subsequently reacted with dust particles to form  
52 nonvolatile salts, resulting in significant nitrate shifts from fine particles into coarse  
53 particles. Such scavenging of fine-particle nitrate led to an enrichment in the daytime  
54 <sup>15</sup>N of nitrate at the mountainside site compared with to the lower-elevation site. In  
55 contrast to nitrate, at the higher elevation, the <sup>15</sup>N in ammonium depleted during the  
56 daytime. Considering the lack of any significant change in ammonia sources during the  
57 vertical transport process, this <sup>15</sup>N depletion in ammonium was mainly the result of



58 unidirectional reactions, indicating that additional ammonia would partition into  
59 particulate phases and further neutralize  $\text{HSO}_4^-$  to form  $\text{SO}_4^{2-}$ . This process would  
60 reduce the aerosol acidity, with a higher pH ( $3.4 \pm 2.2$ ) at MS site and lower ones  
61 ( $2.9 \pm 2.0$ ) at MF site. Our work provides more insight into physicochemical behaviors  
62 of semi-volatile nitrate and ammonium, which will facilitate the improvement in model  
63 for a better simulation of aerosol composition and properties.

64 **Keywords:** Ammonium; Nitrate; Stable nitrogen isotope; Haze; Volatilization

65

66

67

68

69

70

71

72

73

74

75

76

77

78

79



## 80 **1 Introduction**

81 Atmospheric particulate matter measuring equal to or less than 2.5  $\mu\text{m}$  in  
82 aerodynamic diameter ( $\text{PM}_{2.5}$ ) is a worldwide air pollution burden that can deteriorate  
83 the urban air quality and induce adverse human health effects that contribute to  
84 lowering life expectancies (Shiraiwa et al., 2017; Lelieveld et al., 2015; Fuzzi et al.,  
85 2015; Wang et al., 2016). Recent studies have disclosed that the mechanisms underlying  
86 these effects are profoundly dependent on particle properties, e.g., the size,  
87 concentration, mixing state and chemical compositions of particles (Li et al., 2016; Liu  
88 et al., 2021; Guo et al., 2014). Thus, since 2013, China has issued strict emission  
89 directives to mitigate haze pollution. Consequently, the annual  $\text{PM}_{2.5}$  concentration in  
90 China fell by approximately one-third from 2013–2017 (Zheng et al., 2018).  
91 Notwithstanding, the  $\text{PM}_{2.5}$  levels in most cities in China still exceed the least-stringent  
92 target of the World Health Organization (WHO;  $35 \mu\text{g}/\text{m}^3$ ), especially in rural areas and  
93 small cities (Lv et al., 2022; Li et al., 2023).

94 Near-surface PM can also be transported to the upper air, and this process critically  
95 impacts radiative forcing, cloud precipitation and the regional climate by  
96 scattering/absorbing solar radiation and by influencing aerosol-cloud interactions (Van  
97 Donkelaar et al., 2016; Andreae and Ramanathan, 2013; Fan et al., 2018). Past  
98 assessments of these effects have been characterized by large uncertainties (Carslaw et  
99 al., 2013); for example, Bond et al. (2013) found that black carbon climate forcing  
100 varied from  $+0.17 \text{ W}/\text{m}^2$  to  $+2.1 \text{ W}/\text{m}^2$  with a 90% uncertainty. Such massive  
101 uncertainties are mainly due to our limited knowledge regarding the spatiotemporal



102 distribution, abundance and compositions of airborne PM (Seinfeld and Johnh, 2016;  
103 Raes et al., 2000). In addition, aerosols may undergo aging during the vertical transport  
104 process, causing increasingly complex compositions and changes in aerosol properties.  
105 Despite these factors, to date, vertical observations remain comparatively scarce  
106 compared to surface measurements. Therefore, to obtain an improved understanding of  
107 the fundamental chemical and dynamical processes governing haze development, more  
108 field observations of upper-layer aerosols are necessary, as these measurements could  
109 provide updated kinetic and mechanistic parameters that could serve to improve model  
110 simulations.

111 Currently, various monitoring approaches have been developed and applied to  
112 measure vertical aerosols, e.g., satellite remote sensing and in situ lidar methods; these  
113 approaches can be used to obtain the pollution concentration profiles (Van Donkelaar  
114 et al., 2016; Reid et al., 2017). To accurately measure chemical compositions, aircraft  
115 and unmanned aerial vehicles (UAVs) equipped with a variety of instruments can be  
116 utilized in short-term sampling campaigns (Lambey and Prasad, 2021; Zhang et al.,  
117 2017), but these tools are unsuitable for long-term continued observations due to their  
118 high operational costs. In cases of near-surface vertical urban atmosphere observations,  
119 techniques involving tethered balloons, meteorological towers and skyscrapers are  
120 usually adopted (Zhou et al., 2020; Xu et al., 2018; Fan et al., 2021). However, the  
121 vertical application range of these methods are limited to only ~500 m, thus hardly  
122 meeting the requirements of research conducted above the boundary layer. Therefore,  
123 high-elevation mountain sites have long been regarded as suitable places for long-term



124 research on the aerosol chemical compositions and properties and chemical-dynamic  
125 processes that drive haze episodes in the lower troposphere. Although the fixed  
126 observation position is the key drawback of this monitoring approach, it has still been  
127 widely selected for use in various vertical observation campaigns, e.g., in past studies  
128 conducted in Salt Lake Valley (Baasandorj et al., 2017), in Terni Valley (Ferrero et al.,  
129 2012) and on Mt. Tai (Meng et al., 2018; Wang et al., 2011).

130 Mt. Hua adjoins the Guanzhong Basin of inland China, where haze pollution has  
131 been a persistent environmental problem (Wu et al., 2020b; Wu et al., 2021; Wang et  
132 al., 2016). In our previous studies conducted at the mountaintop of Mt. Hua, we found  
133 that air quality was significantly affected by surface pollution, and distinctive  
134 differences were found in the aerosol compositions and size distributions at the  
135 mountaintop compared to those measured at lower elevations ground level (Wang et al.,  
136 2013; Li et al., 2013). With the implementation of strict emission controls, the  
137 atmospheric environment in this region has changed dramatically from the SO<sub>2</sub>/sulfate-  
138 dominated previous environment to the current NO<sub>x</sub>/nitrate-dominated environment  
139 (Baasandorj et al., 2017; Wu et al., 2020c). However, the fundamental chemical and  
140 dynamical processes driving this PM<sub>2.5</sub>-loading explosion are unclear under the current  
141 atmospheric state with increasing O<sub>3</sub> and NH<sub>3</sub> levels. To better rationalize these  
142 processes, in this work, 4-hr integrated aerosol samples were synchronously collected  
143 on the mountainside and at the lower-elevation land surface, and the chemical  
144 components and stable nitrogen isotope compositions of nitrate and ammonium were  
145 analyzed in the collected PM<sub>2.5</sub> samples. We compared the chemical compositions and



146 diurnal cycles between the two sampling sites and then discussed the changes in the  
147 chemical forms of secondary inorganic ions during their vertical transport from lower  
148 to higher elevations. Our study revealed that nitrate and ammonium exhibited distinct  
149 physicochemical behaviors during the aerosol-aging process.

## 150 **2 Experiment**

### 151 **2.1 Sample collection**

152 In this campaign, the PM<sub>2.5</sub> samples were synchronously collected at two locations  
153 in the Mt. Hua area during the period from 27 August to 17 September 2016. One  
154 sampling site was located on a building belonging to the Huashan Meteorological  
155 Bureau (34°32'N, 110°5'E) at the foot of Mt. Hua. Surrounded by several traffic arteries  
156 and dense residential and commercial buildings, as shown in Figure 1b, this site is an  
157 ideal urban station for studying the impacts of anthropogenic activities on local air  
158 quality and is referred to hereafter as the “MF” site. The mountainous sampling site  
159 (34°29'N, 110°3'E) was located approximately 8 km from the city site horizontally  
160 (Figure 1c) at an elevation of 720 m above the average Huashan town level of ~400 m  
161 (a.s.l.). This site was situated on a mountainside that experiences little anthropogenic  
162 activity due to its steep terrain and is abbreviated hereafter as the “MS” site.  
163 Furthermore, this location adjoins one of the larger valleys of Mt. Hua; therefore, the  
164 measurements taken at this location were strongly affected by the lower-elevation air  
165 pollutants transported upwards by the valley winds. At both measurement sites, aerosol  
166 samples were collected at a 4-hr interval in prebaked (at 450°C for 6 hrs) quartz filters  
167 using high-volume (1.13-m<sup>3</sup>/min) air samplers (Tisch Environmental, Inc., USA). All



168 air samplers were installed on the roofs of buildings, approximately 15 m above the  
169 local ground surface. Furthermore, size-resolved aerosol sampling was synchronously  
170 conducted at two sites during summertime (10-22 August, 2020); and these samples  
171 with nine size bins (cutoff points were 0.43, 0.65, 1.1, 2.1, 3.3, 4.7, 5.8 and 9.0  $\mu\text{m}$ ,  
172 respectively) were collected using an Anderson sampler at an airflow rate of 28.3 L/min  
173 for  $\sim 72$  h. After sampling, the filter samples were stored in a freezer (at  $-18^\circ\text{C}$ ) prior to  
174 analysis.

175 The hourly  $\text{PM}_{2.5}$ ,  $\text{NO}_x$ ,  $\text{SO}_2$  and  $\text{O}_3$  mass concentrations were detected at the  
176 mountainside sampling site using an E-BAM, a chemiluminescence analyzer (Thermo,  
177 Model 42i, USA), a pulsed ultraviolet (UV) fluorescence analyzer (Thermo, Model 43i,  
178 USA) and a UV photometric analyzer (Thermo, Model 49i, USA), respectively. At the  
179 MF site, only  $\text{PM}_{2.5}$  was monitored, using another E-BAM, while the data of the other  
180 species were downloaded from the Weinan Ecological Environment Bureau  
181 (<http://sthjj.weinan.gov.cn/>). Meteorological data characterizing both sampling sites  
182 throughout the whole campaign were obtained from the Shaanxi Meteorological Bureau  
183 website (<http://sn.cma.gov.cn/>).

## 184 2.2 Chemical analysis

185 Four punches (1.5-cm diameter) of each aerosol sample were extracted into 10-mL  
186 Milli-Q pure water (18.2 M $\Omega$ ) under sonication for 30 min. Subsequently, the extracts  
187 were filtered with 0.45- $\mu\text{m}$  syringe filters and detected for water-soluble ions ( $\text{Na}^+$ ,  
188  $\text{NH}_4^+$ ,  $\text{K}^+$ ,  $\text{Mg}^{2+}$ ,  $\text{Ca}^{2+}$ ,  $\text{SO}_4^{2-}$ ,  $\text{NO}_2^-$ ,  $\text{NO}_3^-$  and  $\text{Cl}^-$ ) by using ion chromatography; the  
189 detection limit for these nine ions was  $< 0.01 \mu\text{g/mL}$ . A DRI-model 2001 thermal-





190 optical carbon analyzer was used herein following the IMPROVE-A protocol to analyze  
191 the organic carbon (OC) and elemental carbon (EC) in each PM<sub>2.5</sub> filter sample (in  
192 0.526 cm<sup>2</sup> punches). For more details regarding the utilized methods, readers can refer  
193 to our previous studies (Wu et al., 2020b).

194 To quantify the stable nitrogen isotope compositions of nitrate ( $\delta^{15}\text{N-NO}_3^-$ ) and  
195 ammonium ( $\delta^{15}\text{N-NH}_4^+$ ) in PM<sub>2.5</sub> samples, the filter samples were pretreated as  
196 described for the water-soluble ion analysis. The ammonium in the extracts  
197 (approximately half of the resulting solution) was oxidized by hypobromite ( $\text{BrO}^-$ ) to  
198 nitrite ( $\text{NO}_2^-$ ), which was subsequently reduced by hydroxylamine ( $\text{NH}_2\text{OH}$ ) in a  
199 strongly acidic environment. The above product ( $\text{N}_2\text{O}$ ) was then analyzed by a  
200 commercially available purge and cryogenic trap system coupled to an isotope ratio  
201 mass spectrometer (PT-IRMS). A bacterial method (*Pseudomonas aureofaciens*, a  
202 denitrifying bacterium without  $\text{N}_2\text{O}$  reductase activity) was used herein to convert the  
203 sample  $\text{NO}_3^-$  into  $\text{N}_2\text{O}$ , which was ultimately quantified through PT-IRMS. As revealed  
204 in previous studies, the presence of  $\text{NO}_2^-$  in aerosols may interfere with the denitrifier  
205 method when measuring  $\delta^{15}\text{N}$ . Nonetheless,  $\text{NO}_2^-$  generally composed tiny portions in  
206 most of our samples and, on average, contributed <1.0% to  $\text{NO}_3^- + \text{NO}_2^-$ . Thus, we  
207 believed that the proportion of  $\text{NO}_2^-$  in the sample was too small to affect the resulting  
208  $\delta^{15}\text{N}$  measurements based on the discussions reported by Wankel et al. (2010). More  
209 details regarding the analytical artifact and quality control protocols can be found  
210 elsewhere (Wu et al., 2021; Liu et al., 2014).

### 211 **2.3 Concentration-weighted trajectory (CWT) analysis**



212 CWT is a powerful tool used herein to reveal the potential spatial sources responsible  
213 for the high PM<sub>2.5</sub> loadings measured on Mt. Hua; this method has been used previously  
214 in similar studies (Wu et al., 2020c; Wu et al., 2020a). In this study, the CWT analysis  
215 was conducted using the Igor-based tool coupled with hourly PM<sub>2.5</sub> concentrations and  
216 12-hr air mass backward trajectories that were simulated by using the Hybrid-Single  
217 Particle Lagrangian Integrated Trajectory (HYSPLIT) model (Petit et al., 2017).

#### 218 **2.4 Theoretical calculations of the partial pressures of NH<sub>3</sub> and HNO<sub>3</sub> and the** 219 **dissociation constant of NH<sub>4</sub>NO<sub>3</sub>**

220 To obtain the product of the partial pressures of NH<sub>3</sub> and HNO<sub>3</sub>, the NH<sub>4</sub>NO<sub>3</sub>  
221 deliquescence relative humidity (DRH) was first calculated using equation (1) (Eq. 1).  
222 The average DRH of NH<sub>4</sub>NO<sub>3</sub> between the two sites was 65.0±2.9%, slightly lower  
223 than the atmospheric RH (66.0±19.3%). As the works by Wexler and Seinfeld (1991)  
224 and Tang and Munkelwitz (1993) revealed, aerosols are multicomponent mixtures, and  
225 which the aerosol DRH is always lower than the DRH of the individual salts in the  
226 particles. Thus, the actual DRH of the aerosols observed in this study would be lower  
227 than the calculated DRH of NH<sub>4</sub>NO<sub>3</sub>. Based on these analyses, the particles would be  
228 deliquescent most of the time, but for simplification, we always assumed that NH<sub>4</sub>NO<sub>3</sub>  
229 was in an aqueous state, corresponding to the following dissociation reaction (R1):

$$\ln(\text{DRH}) = \frac{723.7}{T} + 1.6954 \quad (\text{Eq. 1})$$
$$\text{NH}_3(\text{g}) + \text{HNO}_3(\text{g}) \rightleftharpoons \text{NH}_4^+ + \text{NO}_3^- \quad (\text{R1})$$

230 According to the approach illustrated in the referenced work (Seinfeld and Johnh,  
231 2016), the equilibrium constant of the dissociation reaction can be described as follows



232 (Eq. 2):

$$K_{AN} = \frac{\gamma_{NH_4NO_3}^2 m_{NH_4^+} m_{NO_3^-}}{P_{HNO_3} P_{NH_3}} \quad (\text{Eq. 2})$$

$$K_{AN} = 4 \times 10^{17} \exp \left\{ 64.7 \left( \frac{298}{T} - 1 \right) + 11.51 \left[ 1 + \ln \left( \frac{298}{T} \right) - \frac{298}{T} \right] \right\} \quad (\text{Eq. 3})$$

$$\ln(K_p) = 118.7 - \frac{24084}{T} - 6.025 \ln(T) \quad (\text{Eq. 4})$$

233 where  $K_{AN}$  ( $\text{mol}^2/(\text{kg}^2 \text{ atm}^2)$ ) is the equilibrium constant of R1 (this value is  
234 temperature-dependent and can be calculated by Eq. 3),  $\gamma_{NH_4NO_3}$  is the binary activity  
235 coefficient for  $NH_4NO_3$  ( $\gamma_{NH_4NO_3} = \gamma_{NH_4^+} \gamma_{NO_3^-}$ ), and  $m_{NH_4^+}$  and  $m_{NO_3^-}$  are the molalities of  
236  $NH_4^+$  and  $NO_3^-$ , respectively. To calculate  $\gamma_{NH_4NO_3}$  and  $m_{NH_4^+} m_{NO_3^-}$ , the activity  
237 coefficients of the corresponding ions and the aerosol water content were assessed using  
238 the E-AIM (IV) model (<http://www.aim.env.uea.ac.uk/aim/model4/model4a.php>).  
239 Combining equations (2) and (3), we obtained the product of the partial pressures of  
240  $NH_3$  and  $HNO_3$  ( $P_{HNO_3} P_{NH_3}$ ), obtaining an average of  $\sim 15.2 \pm 26.0$   $\text{ppb}^2$  at the MF site.  
241 This value was within the range of values ( $1.0 \sim 37.7$   $\text{ppb}^2$ ) measured by the IGAC in  
242 the summer of 2017 in Xi'an, a metropolitan city located in the Guanzhong Basin of  
243 inland China that has suffered from serious haze pollution (Wu et al., 2020a). Thus, we  
244 believe that  $P_{HNO_3} P_{NH_3}$  variations can be assessed using the above method to a certain  
245 extent. Furthermore, the dissociation constant of  $NH_4NO_3$  ( $K_p$ ,  $\text{ppb}^2$ ) can be calculated  
246 as a function of temperature using Eq. 4, as was revealed by Mozurkewich (1993).

### 247 3 Results and discussion

#### 248 3.1 Overview of $PM_{2.5}$ at both sites

##### 249 3.1.1 Meteorological conditions and temporal variations in $PM_{2.5}$ concentrations

250 The temporal variations in the 4-hr  $PM_{2.5}$  mass concentrations, water-soluble ions



251 and meteorological factors measured at the two sampling sites are illustrated in Figure  
252 2, and the comparisons of the above variables are summarized in Table 1. The average  
253 temperature (T) and relative humidity (RH) at the MF site were  $23.2\pm 4.2$  °C and  
254  $68.9\pm 18.2\%$  (Table 1), respectively, and these values were characterized by marked  
255 diurnal variations, as shown in Figure 2a. However, relatively cold and moist weather  
256 frequently occurred at the MS site, which exhibited less pronounced diurnal T and RH  
257 variations, with variations approximately 8 °C and 6% lower than the mean values  
258 derived at the MF site, respectively. Windy weather (wind speed:  $3.2\pm 2.0$  m/s) also  
259 prevailed at this sampling site with gusts above 10.0 m/s; this condition is conducive  
260 to the dissipation of pollutants.

261 Overall, the PM<sub>2.5</sub> concentrations measured at the MF site varied from 22.8 µg/m<sup>3</sup> to  
262 245.6 µg/m<sup>3</sup>, with a mean value of  $76.0\pm 44.1$  µg/m<sup>3</sup>, approximately corresponding to  
263 Grade II (75 µg/m<sup>3</sup>) of the National Ambient Air Quality Standard in China. Even so,  
264 the PM<sub>2.5</sub> levels at Huashan town (i.e., at the MF site) were still higher than those  
265 measured in many typical megacities in the summertime, e.g., Xian (37 µg/m<sup>3</sup> in  
266 2017) (Wu et al., 2020b) and Beijing (46.3 µg/m<sup>3</sup> in 2016) (Lv et al., 2019).

267 Noticeably, stagnant meteorological conditions with increasing RH (> 77%) and  
268 relatively low wind speeds (< 2.0 m/s) occurred during the relatively late stage of  
269 observation, leading to a buildup of high PM<sub>2.5</sub> loadings (78.7 µg/m<sup>3</sup> to 245.6 µg/m<sup>3</sup>).  
270 Such typical haze events last approximately 4 days (12 September to 16 September,  
271 2016), indicating that aerosol pollution is still severe in rural towns despite the notable  
272 air quality improvements recorded in most Chinese urban areas. A similar temporal



273  $PM_{2.5}$  pattern was seen at the MS site, where the average  $PM_{2.5}$  concentration  
274 ( $47.0 \pm 38.0 \mu\text{g}/\text{m}^3$ ) was only 0.62-fold that at the MF site and was within the range of  
275 that measured at the summit of Mt. Tai ( $37.9 \mu\text{g}/\text{m}^3$  in 2016) (Yi et al., 2021) and on  
276 Mt. Lushan ( $55.9 \mu\text{g}/\text{m}^3$  in 2011) (Li et al., 2015) in summertime. As shown in Figure  
277 2d, a multiday episode (mean  $PM_{2.5}$ :  $106.3 \mu\text{g}/\text{m}^3$ ) also appeared at the MS site during  
278 the period from 12 September to 15 September, corresponding to the days on which  
279 high surface pollution was recorded. This was indicative of the potential impacts of  
280 surface pollution on air quality in mountainous areas.

### 281 **3.1.2 Diurnal variation in $PM_{2.5}$**

282 As shown in Figure 2c and 2d, regular diurnal  $PM_{2.5}$  variations were seen throughout  
283 the whole campaign, especially at the MS site. To reveal the differences in the daily  
284 changes in  $PM_{2.5}$  between the two sampling sites, the mean diurnal cycles of hourly  
285  $PM_{2.5}$  and the boundary layer height (BLH) are depicted in Figure 3. At the low-  
286 elevation site, the  $PM_{2.5}$  concentration was moderately enhanced during the nighttime,  
287 with a daily maximum ( $88.2 \pm 53.0 \mu\text{g}/\text{m}^3$ ) observed at 6:00 local standard time (LST).  
288 After sunrise,  $PM_{2.5}$  exhibited a decreasing trend until  $\sim 15:00$  LST, corresponding to  
289 thermally driven boundary-layer growth. Conversely, the aerosol concentrations at the  
290 higher-elevation site immediately increased as the boundary layer uplifted in the early  
291 morning and peaked at 14:00 LST, when the MS site was located completely within the  
292 interior of the boundary layer. Proverbially, anabatic valley winds prevail in  
293 mountainous regions during the daytime. Thus, the aerosol-rich air at MF site may be  
294 transported aloft by the prevailing valley breeze, leading to significantly enhanced



295 PM<sub>2.5</sub> levels at the MS site in short time periods. This finding was further verified by  
296 the similar diurnal NO<sub>2</sub> pattern identified at the MS site, as illustrated in Figure S1. In  
297 the forenoon period, continuous enhancement in the NO<sub>2</sub> level was observed at the MS  
298 site, with a daily maximum of 14.4±53.0 μg/m<sup>3</sup> (at 11:00 LST); this maximum was ~7-  
299 fold the early-morning NO<sub>2</sub> concentration. However, O<sub>3</sub> exhibited indistinctive  
300 variations during this period, and this was indicative of less NO<sub>2</sub> being generated from  
301 photochemical reactions. As mentioned above, there are no obvious anthropogenic  
302 emission sources around the MS site; therefore, our observations indicate the  
303 remarkable transport of pollutants from the lower ground surface to higher elevations  
304 during the daytime.

305 Moreover, the PM<sub>2.5</sub> concentrations at the MS site exhibited less nighttime variation,  
306 with a modest abatement (Figure 3b). The nocturnal BLH usually remained below the  
307 elevation of the MS site; thus, the surface PM<sub>2.5</sub> may have contributed less to the aerosol  
308 levels at the MS site at night. To identify the potential spatial sources of nocturnal PM<sub>2.5</sub>  
309 at the high-elevation site, a high-elevation (CWT) analysis was conducted. As  
310 illustrated in Figure 4, the CWT values in the daylight hours were mostly concentrated  
311 over the sampling site, consistent with our above discussions. However, relatively high  
312 nighttime CWT loadings were distributed on Mt. Hua and in its surrounding regions,  
313 indicating that regional transport may be a major source of PM<sub>2.5</sub> at the MS site at night.  
314 Thus, the constituents of and variations in nocturnal PM<sub>2.5</sub> at the MS site may be mainly  
315 the results of regional features.

### 316 **3.2 Characterization of water-soluble ions in PM<sub>2.5</sub>**



### 317 3.2.1 Comparisons of water-soluble ions between the two sites

318 Figure 5 shows the fractional contributions of the chemical compositions to the  
319  $PM_{2.5}$  at both sampling sites. As summarized in Table 1, the water-soluble ion level  
320 (WSI,  $24.0 \pm 15.0 \mu\text{g}/\text{m}^3$ ) was comparable to that of organic matter (OM,  
321  $OM = 1.6 \times OC$ ) (Wang et al., 2016), with a fractional contribution of  $\sim 31\%$  to  $PM_{2.5}$   
322 (Figure 5). At the higher-elevation site, the WSI exhibited lower values ( $19.5 \pm 16.0$   
323  $\mu\text{g}/\text{m}^3$ ), yet the proportion was moderately enhanced by  $\sim 6\%$ . Notably, this elevated  
324 contribution of WSIs was mostly attributed to secondary inorganic ions (sulfate,  
325 nitrate and ammonium, (SNA)). Similar patterns in which the SNA mass fraction  
326 increased with latitude within the mixing height have also been observed in Terni  
327 Valley (central Italy) (Ferrero et al., 2012) and Salt Lake Valley (US) (Baasandorj et  
328 al., 2017). Among the SNA components, sulfate was the predominant species,  
329 exhibiting slight mass concentration differences between the two sampling sites  
330 ( $10.1 \pm 6.4 \mu\text{g}/\text{m}^3$  versus  $9.0 \pm 7.1 \mu\text{g}/\text{m}^3$ ). However, an  $\sim 4\%$  enhancement in the mass  
331 fraction of sulfate was measured at the higher elevation. Ammonium also exhibited a  
332 similar feature, accounting for  $\sim 5\%$ - $7.5\%$  of the  $PM_{2.5}$ . These sulfate and ammonium  
333 mass concentration homogeneities across the two sites were indicative of the further  
334 formation of these two ions during transport. Unlike sulfate and ammonium, nitrate  
335 and its proportions showed opposite trends, decreasing with elevation; this was  
336 consistent with most of the measured components. Above variation features of SNA  
337 among two sites were found at most of moments in the campaign, except for 12-13  
338 September with a higher SNA concentration at MS site (Figure 2e and 2f). On these



339 two days MS site remained outside the boundary layers (a.s.l., ~550 m), suggesting  
340 less effect of the surface pollutants on the aerosol upper layers. While, the precursor  
341 masses (~12.3  $\mu\text{g}/\text{m}^3$  for  $\text{SO}_2$  and 8.4  $\mu\text{g}/\text{m}^3$  for  $\text{NO}_2$ ) were insufficient to form so  
342 such SNA at MS site. Thus, the higher SNA aloft on above two days may be mostly  
343 driven by regional or long-range transport as indicated by CWT analysis (Figure S2).  
344 Furthermore, distinct nitrate size distributions were also observed between the  
345 different sites in the summertime of 2020. As illustrated in Figure S3, surface nitrate  
346 was enriched in the fine mode, with a minor peak in the coarse fraction. However, the  
347 high-elevation nitrate exhibited a bimodal pattern with two equivalent peaks in the  
348 fine and coarse fractions and was well correlated with coarse mode calcium but  
349 poorly correlated with ammonium ( $R^2=0.51$ ). To our knowledge, ammonium nitrate, a  
350 major form of fine-mode particulate nitrate, can be easily volatilized and converted  
351 into gas-phase  $\text{NH}_3$  and  $\text{HNO}_3$ . Thus, the gaseous  $\text{HNO}_3$  volatilized from fine PM  
352 may react with coarse-modal cations (e.g.,  $\text{Ca}^{2+}$ ,  $\text{Mg}^{2+}$  and  $\text{Na}^+$ ) to form nonvolatile  
353 salts, leading to a significant nitrate shifts from fine particles to large particles. A  
354 similar phenomenon was also found in our previous study conducted at the summit of  
355 Mt. Hua (Wang et al., 2013). Nonvolatile sulfate was predominantly found in the fine  
356 fraction at both sampling sites, which may support this concept. More evidence for  
357 this hypothesis is presented below in section 3.3.

358 The diurnal cycles of the 4-hr sulfate, nitrate and ammonium are illustrated in  
359 Figure S4. As shown in Figure S4, the total SNA concentration at the MF site  
360 exhibited a morning peak from 8:00-12:00 LST; this variation was quite different





361 from that of  $PM_{2.5}$ . Such a difference between the total SNA and  $PM_{2.5}$  at the MF site  
362 could partially be attributed to the lower sampling resolution and enhanced formation  
363 of SNA in the morning. The diurnal total SNA pattern identified at the MS site  
364 coincided with the  $PM_{2.5}$  pattern, exhibiting a daily maximum reaching  $\sim 25.0 \pm 18.0$   
365  $\mu\text{g}/\text{m}^3$  (from 12:00-16:00 LST), a 1.2-fold increase compared to that measured at the  
366 MF site. Among the SNA components, morning peaks of nitrate and ammonium (from  
367 8:00-12:00 LST) were also observed at the MF site. Through vertical transport, the  
368 surface nitrate and ammonium can contribute to that at the MS site, leading to a  
369 significant enhancement in nitrate and ammonium concentrations aloft with the  
370 afternoon peaks during 12:00-16:00 LST. Even so, the maximum nitrate concentration  
371 at the MS site ( $8.1 \pm 8.7 \mu\text{g}/\text{m}^3$ ) was still lower than that measured at the MF site  
372 ( $9.8 \pm 8.0 \mu\text{g}/\text{m}^3$ ) due to the  $\text{NH}_4\text{NO}_3$  volatilization under the transport process, while  
373 ammonium exhibited the opposite trend. This finding was consistent with the above  
374 discussion. Unlike nitrate and ammonium, similar diurnal variations in sulfate were  
375 observed between the two sampling sites, with daily maxima observed from 12:00-  
376 16:00 at both sites. The major sulfate formation pathway during the daytime in  
377 summer is the photooxidation of  $\text{SO}_2$  with an OH radical, and the formation rate  
378 facilitated by this process is much lower than that of the nitrate formation process  
379 (Seinfeld and Johnh, 2016; Rodhe et al., 1981). Thus, sulfate formation may occur  
380 continuously during vertical transport, leading to smaller difference in the diurnal  
381 cycle of sulfate between the two sites.

### 382 **3.2.2 Chemical forms of SNA at both sites**



383 As shown in Figure 5, the water-soluble ions considered herein mainly included  
384 sulfate, nitrate and ammonium, which usually exist in the form of ammonium salts  
385 ( $\text{NH}_4\text{HSO}_4$ ,  $(\text{NH}_4)_2\text{SO}_4$ ,  $\text{NH}_4\text{NO}_3$ , and so on). In the  $\text{H}_2\text{SO}_4$ - $\text{HNO}_3$ - $\text{NH}_3$   
386 thermodynamic system,  $\text{H}_2\text{SO}_4$  and  $\text{HNO}_3$  are neutralized by ammonia under  
387 ammonia-rich conditions and mainly exist as  $(\text{NH}_4)_2\text{SO}_4$  and  $\text{NH}_4\text{NO}_3$  in aerosols.  
388 Conversely,  $\text{H}_2\text{SO}_4$  is converted to  $\text{HSO}_4^-$  in environments with relatively low  $\text{NH}_3$   
389 availabilities. Thus,  $\text{NH}_4\text{HSO}_4$  and  $\text{NH}_4\text{NO}_3$  may be the dominant aerosol components  
390 under such environmental conditions (Rodhe et al., 1981; Seinfeld and Johnh, 2016).  
391 To reveal the major SNA forms at the different sampling sites considered herein, the  
392 theoretical ammonium concentration was calculated according to thermodynamic  
393 equilibrium with the atmospheric sulfate and nitrate levels. The theoretical  
394 ammonium levels were calculated as follows:

$$\text{NH}_4^+_{\text{theory}} = \left( \frac{[\text{SO}_4^{2-}]}{48} + \frac{[\text{NO}_3^-]}{62} \right) \times 18 \quad (\text{Eq. 5})$$

$$\text{NH}_4^+_{\text{theory}} = \left( \frac{[\text{SO}_4^{2-}]}{96} + \frac{[\text{NO}_3^-]}{62} \right) \times 18 \quad (\text{Eq. 6})$$

395 where  $[\text{SO}_4^{2-}]$  and  $[\text{NO}_3^-]$  represent atmospheric concentrations ( $\mu\text{g}/\text{m}^3$ ). When  
396  $(\text{NH}_4)_2\text{SO}_4$  and  $\text{NH}_4\text{NO}_3$  are the dominant species, the  $\text{NH}_4^+_{\text{theory}}$  can be calculated  
397 using equation (5). In contrast, equation (6) suggests that  $\text{NH}_4\text{HSO}_4$  and  $\text{NH}_4\text{NO}_3$  are  
398 abundantly present in the analyzed aerosols. Figure 6 compares the measured  $\text{NH}_4^+$   
399 concentrations with the theoretical  $\text{NH}_4^+$  concentrations derived by the two equations  
400 above. As illustrated in Figure 6(a), the slope of the observational  $\text{NH}_4^+$  values against  
401 the theoretical  $\text{NH}_4^+$  values calculated using equation (6) was much closer to one at the  
402 MF site than at the MS site, meaning that  $\text{NH}_4\text{HSO}_4$  and  $\text{NH}_4\text{NO}_3$  were the major



403 chemical forms of SNA at MF site. However, the opposite pattern was revealed at the  
404 higher-elevation site; thus, the upper aerosols were characterized by abundant  
405  $(\text{NH}_4)_2\text{SO}_4$  and  $\text{NH}_4\text{NO}_3$ . Such chemical compositions of aerosols at the MS site were  
406 unexpected under the relatively ammonia-poor environment; the ammonia level at this  
407 site was only  $\sim 10\%$  that at the MF site (according to observational data collected during  
408 the 2020 summertime). As can be inferred from earlier studies, the ammonia Henry's  
409 law coefficients generally increase in value as the temperature decreases. Therefore, the  
410 lower temperatures measured at the MS site would create a more favorable environment  
411 for ammonia, thus shifting its partitioning toward the particulate phase. The  $\text{HSO}_4^-$   
412 transported from the MF site would thus be further neutralized to  $\text{SO}_4^{2-}$  by this  
413 additional ammonium during transport, leading to the significant difference observed  
414 in the chemical forms of SNA between the two sites. Moreover, as the chemical  
415 component change from  $\text{NH}_4\text{HSO}_4$  to  $(\text{NH}_4)_2\text{SO}_4$ , the aerosol acidity moderately  
416 decreased, showing a higher bulk  $\text{PM}_{2.5}$  pH ( $3.4 \pm 2.2$ ) at relatively clean upper layer  
417 and a lower value ( $2.9 \pm 2.0$ ) at heavily polluted grounds (Table 1). However, the  
418 previous studies were generally recognized that the aerosol would become more acidic  
419 when the air parcels were transported from the polluted to cleaner/remote regions (Liu  
420 et al., 1996; Nault et al., 2021). Such a reduced aerosol acidity with increasing elevation  
421 in our study was mainly due to the different physicochemical behaviors of the semi-  
422 volatile species nitrate and ammonium, more discussions are included in the following  
423 section.

### 424 3.3 Physicochemical behaviors of nitrate and ammonium during transport



425 According to the above discussion, a conceptual model illustrating the  
426 physicochemical behaviors of nitrate and ammonium during vertical transport was  
427 proposed to explain the chemical composition differences between the two sites. As  
428 shown in Figure 7, surface air parcels containing abundant  $\text{NH}_4\text{HSO}_4$  and  $\text{NH}_4\text{NO}_3$   
429 particles can be transported to the upper atmosphere by the prevailing valley winds,  
430 and during this process, the volatile  $\text{NH}_4\text{NO}_3$  is easily converted to gaseous  $\text{NH}_3$  and  
431  $\text{HNO}_3$ . Subsequently, heterogeneous reactions of the gaseous  $\text{HNO}_3$  with fugitive dust  
432 occur, thus forming nonvolatile salts and resulting in the accumulation of nitrate on  
433 the coarse-mode particles. However, as the temperature decreased, the ammonia that  
434 volatilized from the fine particles or was derived from the surface can re-enter the  
435 particulate phase through the gas–particle partition. Therefore,  $(\text{NH}_4)_2\text{SO}_4$  would be  
436 formed in the aerosol phase and would gradually replace  $\text{NH}_4\text{HSO}_4$ .

437 To investigate the likelihood of  $\text{NH}_4\text{NO}_3$  volatilization during the transport process,  
438 the dissociation constant of  $\text{NH}_4\text{NO}_3$  ( $K_p$ ) and the partial pressures of gas-phase  $\text{NH}_3$   
439 and  $\text{HNO}_3$  were calculated in this study. More details regarding the calculation steps  
440 of the above factors can be found in section 2.4. Based on the thermodynamic  
441 principles presented by Stelson and Seinfeld (1982), when the product of the partial  
442 pressures of  $\text{NH}_3$  and  $\text{HNO}_3$  ( $P_{\text{HNO}_3} \times P_{\text{NH}_3}$ ) is greater than  $K_p$ , the equilibrium of the  
443 system shifts toward the aerosol phase, thus increasing  $\text{NH}_4\text{NO}_3$  formation. In  
444 contrast, a relatively low  $P_{\text{HNO}_3} \times P_{\text{NH}_3} / K_p$  value ( $<1$ ) suggests that  $\text{NH}_4\text{NO}_3$   
445 dissociation is induced and that  $\text{NH}_4\text{NO}_3$  is transferred to the gas phase. Figure 8  
446 depicts the ratio of the product of the partial pressures of  $\text{NH}_3$  and  $\text{HNO}_3$  with



447 different ambient temperatures. As shown in Figure 8, approximately 85% of the  
448 samples collected at both sampling sites were located within the region with  
449  $P_{\text{HNO}_3} \times P_{\text{NH}_3} / K_p$  less than 1, demonstrating a common  $\text{NH}_4\text{NO}_3$  dissociation  
450 phenomenon during the observed period. For the samples with  $P_{\text{HNO}_3} \times P_{\text{NH}_3} / K_p$  ratios  
451  $< 1$ , the mean value of the MS-site ratios was approximately half that of the MF-site  
452 ratios, indicating that  $\text{NH}_4\text{NO}_3$  dissociation may be more likely at higher elevations  
453 that at lower elevations. This finding was inconsistent with the aircraft observations  
454 collected in the western U.S. by Lindaas et al. (2021), who revealed that  
455  $P_{\text{HNO}_3} \times P_{\text{NH}_3} / K_p$  exhibited an increasing trend within 3 km (a.s.l.).

456 Moreover, the nitrogen isotope compositions of nitrate and ammonium in  $\text{PM}_{2.5}$   
457 were measured to further verify the conceptual model. As previously mentioned,  
458 unlike daytime pollutants, nocturnal pollutants exhibited different sources between the  
459 two sampling sites. Thus, their nitrogen isotope compositions were more complicated  
460 and less comparable. However, for simplicity, only the daytime samples were  
461 analyzed herein based on the hypothesis that the sources of the high-elevation  
462 pollutants were the same as those of the pollutants collected at the MF site. As shown  
463 in Figure 9, a discrepancy in the  $\delta^{15}\text{N}$  value of nitrate ( $\delta^{15}\text{N}\text{-NO}_3^-$ ) featuring more  $^{15}\text{N}$ -  
464 enriched  $\text{NO}_3^-$  was observed at the higher elevation, with a  $p$  value less than 0.05.

465 This finding can be ascribed to the evaporation of a portion of the particulate  $\text{NH}_4\text{NO}_3$   
466 due to a dissociation shift in equilibrium; in this shift, the lighter  $^{14}\text{N}$  was  
467 preferentially incorporated into the atmosphere, leading to  $^{15}\text{N}$  enrichment in the  
468 remaining nitrate. Additionally, Freyer et al. (1993) revealed that gas-phase isotopic



469 exchanges between NO and NO<sub>2</sub> result in the enrichment of the heavier <sup>15</sup>N isotope in  
470 the more oxidized form and may further affect δ<sup>15</sup>N-NO<sub>3</sub><sup>-</sup> through nitrate formation  
471 reactions. The above isotopic exchange between NO<sub>2</sub> and NO<sub>x</sub> can be roughly  
472 described as follows: [δ<sup>15</sup>N(NO<sub>2</sub>)-δ<sup>15</sup>N(NO<sub>x</sub>)]=(1- K)×(1-f<sub>NO2</sub>), where K and f<sub>NO2</sub> are  
473 the temperature-dependent exchange constant and mole fraction of NO<sub>2</sub>, respectively.  
474 Based on trace gas observations, the f<sub>NO2</sub> values of the air aloft were very high due to  
475 the frequently undetectable NO concentration, indicating a rather limited isotopic  
476 exchange between NO<sub>2</sub> and NO. Therefore, the evaporation of particulate NH<sub>4</sub>NO<sub>3</sub>  
477 have been the significant factor affecting the measurement of a higher δ<sup>15</sup>N-NO<sub>3</sub><sup>-</sup> at  
478 the MS site than at the MF site in our observations. According to the above analysis,  
479 the ammonium at higher elevation should theoretically be more and more enriched in  
480 δ<sup>15</sup>N with the continuous NH<sub>4</sub>NO<sub>3</sub> volatilization. However, our observation of δ<sup>15</sup>N-  
481 NH<sub>4</sub><sup>+</sup> did not correspond to above pattern, namely, ammonium at the MS site depleted  
482 in δ<sup>15</sup>N compared to that at MF site (*p*<0.05, Figure 9). Given the unchanged  
483 ammonia sources, such seemingly unreasonable observations were mainly caused by  
484 the gas-to-particle conversion of ammonia. In this process, the reversible phase-  
485 equilibrium reactions between NH<sub>3</sub>(g) and HNO<sub>3</sub>(g)/HCl(g) would yield positive  
486 enrichment in δ<sup>15</sup>N of aerosol NH<sub>4</sub><sup>+</sup> (Walters et al., 2019); nevertheless, unidirectional  
487 reactions involving NH<sub>3</sub>(g) and SO<sub>4</sub><sup>2-</sup>/HSO<sub>4</sub><sup>-</sup> favored <sup>15</sup>N depletion in the particle  
488 form as revealed by Heaton et al. (1997). Thereby, the lower δ<sup>15</sup>N-NH<sub>4</sub><sup>+</sup> values at MS  
489 site were mostly driven by those irreversible reactions, rather than the reversible  
490 equilibrium ones. This result further confirmed our conjecture that the additional



491 ammonia would partition into particulate phases and further neutralize the acidic  
492  $\text{NH}_4\text{HSO}_4$ , leading to an increasing pH at MS site compared to that at MF site. Taken  
493 together, this compelling evidence verifies that fine-mode nitrate and ammonium  
494 exhibit distinctly different physicochemical behaviors during their transport.

#### 495 **4 Conclusions and atmospheric implications**

496 In this study, aerosol samples were collected at 4-hr intervals on the mountainside  
497 of Mt. Hua, and the OC, EC, water-soluble ions and isotope compositions of nitrate  
498 and ammonium were measured and compared with simultaneous observations taken  
499 at a lower-elevation site (MF site). The particle mass at the MF site was  
500 approximately 1.5-fold that at the higher elevation, and distinctly different diurnal  
501 cycles were observed between the two sampling sites. Based on the BLH variation,  
502 we revealed that near-surface  $\text{PM}_{2.5}$  could be transported to the upper layers by the  
503 mountain-valley breeze, leading to the gradual accumulation of pollutants on the  
504 mountainside during the daytime.

505 Sulfate, the predominant species found among ions at both sampling sites,  
506 exhibited nearly identical mass concentrations at the two sites but had a moderately  
507 enhanced mass fraction at the higher elevation. Such homogeneity was also observed  
508 in ammonium, which mainly existed as  $\text{NH}_4\text{HSO}_4+\text{NH}_4\text{NO}_3$  and  
509  $(\text{NH}_4)_2\text{SO}_4+\text{NH}_4\text{NO}_3$  at the lower- and higher-elevation sites, respectively. This  
510 observation indicated the further formation of ammonium during the transport  
511 process. Unlike sulfate and ammonium, nitrate at the MS site exhibited abated trends  
512 in both its concentration and proportion, mainly due to the volatilization of  $\text{NH}_4\text{NO}_3$ .



513 With the help of nitrate and ammonium nitrogen isotopes, we proposed a conceptual  
514 model to illustrate the different behaviors of nitrate and ammonium during vertical  
515 transport; in this model, the semivolatile  $\text{NH}_4\text{NO}_3$  in surface air parcels was easily  
516 converted into gaseous  $\text{NH}_3$  and  $\text{HNO}_3$ . Subsequently, heterogeneous reactions  
517 occurred between this gaseous  $\text{HNO}_3$  and fugitive dust, forming nonvolatile salts and  
518 leading to a significant nitrate shift from fine particles into coarse particles. In  
519 addition, the decreasing temperature was favorable for ammonia partitioning toward  
520 the particle phase, and the addition of ammonium further neutralized  $\text{HSO}_4^-$  to form  
521  $\text{SO}_4^{2-}$ . This process would reduce the aerosol acidity, with bulk  $\text{PM}_{2.5}$  pH increasing  
522 from  $2.9 \pm 2.0$  at MF site to  $3.4 \pm 2.2$  at MS site.

523 Over the past decade, the relative abundance of  $\text{NH}_4\text{NO}_3$  has been enhanced in  
524 most urban areas of China because strict emission directives have been promulgated  
525 to abate the emission and environmental impacts of  $\text{SO}_2$  (Xie et al., 2020; Song et al.,  
526 2019). In this work, we observed that  $\text{NH}_4\text{NO}_3$  volatilization was a ubiquitous  
527 phenomenon for particles during transport, resulting in a shift in partwise nitrate from  
528 the fine mode to the coarse fraction; this shift has also been reported in the offshore  
529 areas of the UK (Yeatman et al., 2001). Thus, we think that considering only fine-  
530 fraction nitrate may result in the conversion rate of  $\text{NO}_x$  to nitrate being partly  
531 underestimated at some times, especially in the summer. Moreover, the deposition  
532 velocity of coarse particles is usually faster than that of fine particles; therefore, the  
533 above process would appreciably elevate the deposition of N into the environment.  
534 Indeed, abundant  $\text{NO}_2$ ,  $\text{O}_3$  and  $\text{NH}_3$  co-occurrence is common in the East Asian





535 atmosphere, and under these conditions, secondary inorganic aerosols can be  
536 effectively produced, leading to a PM<sub>2.5</sub> loading explosion in the urban atmosphere of  
537 China (Wu et al., 2020c; Wang et al., 2016). Given this, harmonious reductions in  
538 NO<sub>2</sub>, O<sub>3</sub> and NH<sub>3</sub> will be urgent in further mitigation strategies to improve air quality  
539 and alleviate other potential effects.

540

541 **Author contributions.** GW designed the experiment. CW, JiaL and CC collected the  
542 samples. CW and CC conducted the experiments. CW and GW performed the data  
543 interpretation and wrote the paper. All authors contributed to the paper with useful  
544 scientific discussions or comments.

545

546 **Competing interests.** The authors declare that they have no conflict of interest.

547

548 **Acknowledgements.** This work was financially supported by the National Natural  
549 Science Foundation of China (No. 42130704, 42007202), Shanghai Science and  
550 Technology Innovation Action Plan (20dz1204000) and ECNU Happiness Flower  
551 program.

552

553

554

## 555 **References**

- 556 Andreae, M. O. and Ramanathan, V.: Climate's Dark Forcings, *Science*, 340, 280-281,  
557 10.1126/science.1235731, 2013.
- 558 Baasandorj, M., Hoch, S. W., Bares, R., Lin, J. C., Brown, S. S., Millet, D. B., Martin, R., Kelly, K.,  
559 Zarzana, K. J., Whiteman, C. D., Dube, W. P., Tonnesen, G., Jaramillo, I. C., and Sohl, J.: Coupling  
560 between Chemical and Meteorological Processes under Persistent Cold-Air Pool Conditions:  
561 Evolution of Wintertime PM<sub>2.5</sub> Pollution Events and N<sub>2</sub>O<sub>5</sub> Observations in Utah's Salt Lake Valley,



- 562 Environ. Sci. Technol., 51, 5941-5950, 10.1021/acs.est.6b06603, 2017.
- 563 Bond, T. C., Doherty, S. J., Fahey, D. W., Forster, P. M., Bernsten, T., DeAngelo, B. J., Flanner, M. G.,  
564 Ghan, S., Kaercher, B., Koch, D., Kinne, S., Kondo, Y., Quinn, P. K., Sarofim, M. C., Schultz, M.  
565 G., Schulz, M., Venkataraman, C., Zhang, H., Zhang, S., Bellouin, N., Guttikunda, S. K., Hopke, P.  
566 K., Jacobson, M. Z., Kaiser, J. W., Klimont, Z., Lohmann, U., Schwarz, J. P., Shindell, D., Storelvmo,  
567 T., Warren, S. G., and Zender, C. S.: Bounding the role of black carbon in the climate system: A  
568 scientific assessment, *J. Geophys. Res.-Atmos.*, 118, 5380-5552, 10.1002/jgrd.50171, 2013.
- 569 Carslaw, K. S., Lee, L. A., Reddington, C. L., Pringle, K. J., Rap, A., Forster, P. M., Mann, G. W.,  
570 Spracklen, D. V., Woodhouse, M. T., Regayre, L. A., and Pierce, J. R.: Large contribution of natural  
571 aerosols to uncertainty in indirect forcing, *Nat.*, 503, 67-+, 10.1038/nature12674, 2013.
- 572 Fan, J., Rosenfeld, D., Zhang, Y., Giangrande, S. E., Li, Z., Machado, L. A. T., Martin, S. T., Yang, Y.,  
573 Wang, J., Artaxo, P., Barbosa, H. M. J., Braga, R. C., Comstock, J. M., Feng, Z., Gao, W., Gomes,  
574 H. B., Mei, F., Poehlker, C., Poehlker, M. L., Poeschl, U., and de Souza, R. A. F.: Substantial  
575 convection and precipitation enhancements by ultrafine aerosol particles, *Science*, 359, 411-+,  
576 10.1126/science.aan8461, 2018.
- 577 Fan, M.-Y., Zhang, Y.-L., Lin, Y.-C., Hong, Y., Zhao, Z.-Y., Xie, F., Du, W., Cao, F., Sun, Y., and Fu, P.:  
578 Important Role of NO<sub>3</sub> Radical to Nitrate Formation Aloft in Urban Beijing: Insights from Triple  
579 Oxygen Isotopes Measured at the Tower, *Environ. Sci. Technol.*, 10.1021/acs.est.1c02843, 2021.
- 580 Ferrero, L., Cappelletti, D., Moroni, B., Sangiorgi, G., Perrone, M. G., Crocchianti, S., and Bolzacchini,  
581 E.: Wintertime aerosol dynamics and chemical composition across the mixing layer over basin  
582 valleys, *Atmos. Environ.*, 56, 143-153, 10.1016/j.atmosenv.2012.03.071, 2012.
- 583 Freyer, H. D., Kley, D., Volz-Thomas, A., and Kobel, K.: On the interaction of isotopic exchange  
584 processes with photochemical reactions in atmospheric oxides of nitrogen, *Journal of Geophysical*  
585 *Research*, 98, 14791-14796, 10.1029/93jd00874, 1993.
- 586 Fuzzi, S., Baltensperger, U., Carslaw, K., Decesari, S., van der Gon, H. D., Facchini, M. C., Fowler, D.,  
587 Koren, I., Langford, B., Lohmann, U., Nemitz, E., Pandis, S., Riipinen, I., Rudich, Y., Schaap, M.,  
588 Slowik, J. G., Spracklen, D. V., Vignati, E., Wild, M., Williams, M., and Gilardoni, S.: Particulate  
589 matter, air quality and climate: lessons learned and future needs, *Atmos. Chem. Phys.*, 15, 8217-  
590 8299, 10.5194/acp-15-8217-2015, 2015.
- 591 Guo, S., Hu, M., Zamora, M. L., Peng, J., Shang, D., Zheng, J., Du, Z., Wu, Z., Shao, M., Zeng, L.,  
592 Molina, M. J., and Zhang, R.: Elucidating severe urban haze formation in China, *Proc. Natl. Acad.*  
593 *Sci. USA*, 111, 17373-17378, 10.1073/pnas.1419604111, 2014.
- 594 Heaton, T. H. E., Spiro, B., Madeline, S., and Robertson, C.: Potential canopy influences on the isotopic  
595 composition of nitrogen and sulphur in atmospheric deposition, *Oecologia*, 109, 600-607,  
596 10.1007/s004420050122, 1997.
- 597 Lambey, V. and Prasad, A. D.: A Review on Air Quality Measurement Using an Unmanned Aerial Vehicle,  
598 *Water, Air, & Soil Pollution*, 232, 10.1007/s11270-020-04973-5, 2021.
- 599 Lelieveld, J., Evans, J. S., Fnais, M., Giannadaki, D., and Pozzer, A.: The contribution of outdoor air  
600 pollution sources to premature mortality on a global scale, *Nat.*, 525, 367-+, 10.1038/nature15371,  
601 2015.
- 602 Li, D., Wu, C., Zhang, S., Lei, Y., Lv, S., Du, W., Liu, S., Zhang, F., Liu, X., Liu, L., Meng, J., Wang, Y.,  
603 Gao, J., and Wang, G.: Significant coal combustion contribution to water-soluble brown carbon  
604 during winter in Xingtai, China: Optical properties and sources, *J. Environ. Sci.*, 124, 892-900,  
605 10.1016/j.jes.2022.02.026, 2023.



- 606 Li, J. J., Wang, G. H., Cao, J. J., Wang, X. M., and Zhang, R. J.: Observation of biogenic secondary  
607 organic aerosols in the atmosphere of a mountain site in central China: temperature and relative  
608 humidity effects, *Atmos. Chem. Phys.*, 13, 11535-11549, 10.5194/acp-13-11535-2013, 2013.
- 609 Li, T., Wang, Y., Li, W. J., Chen, J. M., Wang, T., and Wang, W. X.: Concentrations and solubility of trace  
610 elements in fine particles at a mountain site, southern China: regional sources and cloud processing,  
611 *Atmos. Chem. Phys.*, 15, 8987-9002, 10.5194/acp-15-8987-2015, 2015.
- 612 Li, W., Shao, L., Zhang, D., Ro, C.-U., Hu, M., Bi, X., Geng, H., Matsuki, A., Niu, H., and Chen, J.: A  
613 review of single aerosol particle studies in the atmosphere of East Asia: morphology, mixing state,  
614 source, and heterogeneous reactions, *Journal of Cleaner Production*, 112, 1330-1349,  
615 10.1016/j.jclepro.2015.04.050, 2016.
- 616 Lindaas, J., Pollack, I. B., Calahorrano, J. J., O'Dell, K., Garofalo, L. A., Pothier, M. A., Farmer, D. K.,  
617 Kreidenweis, S. M., Campos, T., Flocke, F., Weinheimer, A. J., Montzka, D. D., Tyndall, G. S., Apel,  
618 E. C., Hills, A. J., Hornbrook, R. S., Palm, B. B., Peng, Q., Thornton, J. A., Permar, W., Wielgasz,  
619 C., Hu, L., Pierce, J. R., Collett, J. L., Jr., Sullivan, A. P., and Fischer, E. V.: Empirical Insights Into  
620 the Fate of Ammonia in Western US Wildfire Smoke Plumes, *J. Geophys. Res.-Atmos.*, 126,  
621 10.1029/2020jd033730, 2021.
- 622 Liu, D., Fang, Y., Tu, Y., and Pan, Y.: Chemical Method for Nitrogen Isotopic Analysis of Ammonium at  
623 Natural Abundance, *Anal. Chem.*, 86, 3787-3792, 10.1021/ac403756u, 2014.
- 624 Liu, L. J. S., Burton, R., Wilson, W. E., and Koutrakis, P.: Comparison of aerosol acidity in urban and  
625 semirural environments, *Atmos. Environ.*, 30, 1237-1245, 10.1016/1352-2310(95)00438-6, 1996.
- 626 Liu, T., Chan, A. W. H., and Abbatt, J. P. D.: Multiphase Oxidation of Sulfur Dioxide in Aerosol Particles:  
627 Implications for Sulfate Formation in Polluted Environments, *Environ. Sci. Technol.*, 55, 4227-4242,  
628 10.1021/acs.est.0c06496, 2021.
- 629 Lv, D., Chen, Y., Zhu, T., Li, T., Shen, F., Li, X., and Mehmood, T.: The pollution characteristics of PM10  
630 and PM2.5 during summer and winter in Beijing, Suning and Islamabad, *Atmospheric Pollution*  
631 *Research*, 10, 1159-1164, 10.1016/j.apr.2019.01.021, 2019.
- 632 Lv, S., Wang, F., Wu, C., Chen, Y., Liu, S., Zhang, S., Li, D., Du, W., Zhang, F., Wang, H., Huang, C.,  
633 Fu, Q., Duan, Y., and Wang, G.: Gas-to-Aerosol Phase Partitioning of Atmospheric Water-Soluble  
634 Organic Compounds at a Rural Site in China: An Enhancing Effect of NH<sub>3</sub> on SOA Formation,  
635 *Environ. Sci. Technol.*, 56, 3915-3924, 10.1021/acs.est.1c06855, 2022.
- 636 Meng, J., Wang, G., Hou, Z., Liu, X., Wei, B., Wu, C., Cao, C., Wang, J., Li, J., Cao, J., Zhang, E., Dong,  
637 J., Liu, J., Ge, S., and Xie, Y.: Molecular distribution and stable carbon isotopic compositions of  
638 dicarboxylic acids and related SOA from biogenic sources in the summertime atmosphere of Mt.  
639 Tai in the North China Plain, *Atmos. Chem. Phys.*, 18, 15069-15086, 10.5194/acp-18-15069-2018,  
640 2018.
- 641 Mozurkewich, M.: The dissociation constant of ammonium nitrate and its dependence on temperature,  
642 relative humidity and particle size, *Atmospheric Environment. Part A. General Topics*, 27, 261-270,  
643 1993.
- 644 Nault, B. A., Campuzano-Jost, P., Day, D. A., Jo, D. S., Schroder, J. C., Allen, H. M., Bahreini, R., Bian,  
645 H., Blake, D. R., Chin, M., Clegg, S. L., Colarco, P. R., Crouse, J. D., Cubison, M. J., DeCarlo, P.  
646 F., Dibb, J. E., Diskin, G. S., Hodzic, A., Hu, W., Katich, J. M., Kim, M. J., Kodros, J. K., Kupc, A.,  
647 Lopez-Hilfiker, F. D., Marais, E. A., Middlebrook, A. M., Andrew Neuman, J., Nowak, J. B., Palm,  
648 B. B., Paulot, F., Pierce, J. R., Schill, G. P., Scheuer, E., Thornton, J. A., Tsigaridis, K., Wennberg,  
649 P. O., Williamson, C. J., and Jimenez, J. L.: Chemical transport models often underestimate



- 650 inorganic aerosol acidity in remote regions of the atmosphere, *Communications Earth &*  
651 *Environment*, 2, 10.1038/s43247-021-00164-0, 2021.
- 652 Petit, J. E., Favez, O., Albinet, A., and Canonaco, F.: A user-friendly tool for comprehensive evaluation  
653 of the geographical origins of atmospheric pollution: Wind and trajectory analyses, *Environmental*  
654 *Modelling & Software*, 88, 183-187, 10.1016/j.envsoft.2016.11.022, 2017.
- 655 Raes, F., Van Dingenen, R., Vignati, E., Wilson, J., Putaud, J. P., Seinfeld, J. H., and Adams, P.: Formation  
656 and cycling of aerosols in the global troposphere, *Atmos. Environ.*, 34, 4215-4240, 10.1016/s1352-  
657 2310(00)00239-9, 2000.
- 658 Reid, J. S., Kuehn, R. E., Holz, R. E., Eloranta, E. W., Kaku, K. C., Kuang, S., Newchurch, M. J.,  
659 Thompson, A. M., Trepte, C. R., Zhang, J., Atwood, S. A., Hand, J. L., Holben, B. N., Minnis, P.,  
660 and Posselt, D. J.: Ground-based High Spectral Resolution Lidar observation of aerosol vertical  
661 distribution in the summertime Southeast United States, *J. Geophys. Res.-Atmos.*, 122, 2970-3004,  
662 10.1002/2016jd025798, 2017.
- 663 Rodhe, H., Crutzen, P., and Vanderpol, A.: Formation of sulfuric and nitric acid in the atmosphere during  
664 long-range transport, *Tellus*, 33, 132-141, 1981.
- 665 Seinfeld and JohnH: Atmospheric chemistry and physics : from air pollution to climate change / 3nd ed,  
666 Atmospheric chemistry and physics : from air pollution to climate change / 3nd ed2016.
- 667 Shiraiwa, M., Ueda, K., Pozzer, A., Lammel, G., Kampf, C. J., Fushimi, A., Enami, S., Arangio, A. M.,  
668 Froehlich-Nowoisky, J., Fujitani, Y., Furuyama, A., Lakey, P. S. J., Lelieveld, J., Lucas, K., Morino,  
669 Y., Poeschl, U., Takahama, S., Takami, A., Tong, H., Weber, B., Yoshino, A., and Sato, K.: Aerosol  
670 Health Effects from Molecular to Global Scales, *Environ. Sci. Technol.*, 51, 13545-13567,  
671 10.1021/acs.est.7b04417, 2017.
- 672 Song, S., Nenes, A., Gao, M., Zhang, Y., Liu, P., Shao, J., Ye, D., Xu, W., Lei, L., Sun, Y., Liu, B., Wang,  
673 S., and McElroy, M. B.: Thermodynamic Modeling Suggests Declines in Water Uptake and Acidity  
674 of Inorganic Aerosols in Beijing Winter Haze Events during 2014/2015-2018/2019, *Environmental*  
675 *Science & Technology Letters*, 6, 752-760, 10.1021/acs.estlett.9b00621, 2019.
- 676 Stelson, A. W. and Seinfeld, J. H.: Relative humidity and temperature dependence of the ammonium  
677 nitrate dissociation constant, *Atmos. Environ.*, 16, 983-992, 10.1016/0004-6981(82)90184-6, 1982.
- 678 Tang, I. N. and Munkelwitz, H. R.: Composition and temperature dependence of the deliquescence  
679 properties of hygroscopic aerosols, *Atmos. Environ.*, 27, 467-473, 1993.
- 680 van Donkelaar, A., Martin, R. V., Brauer, M., Hsu, N. C., Kahn, R. A., Levy, R. C., Lyapustin, A., Sayer,  
681 A. M., and Winker, D. M.: Global Estimates of Fine Particulate Matter using a Combined  
682 Geophysical-Statistical Method with Information from Satellites, Models, and Monitors, *Environ.*  
683 *Sci. Technol.*, 50, 3762-3772, 10.1021/acs.est.5b05833, 2016.
- 684 Walters, W. W., Chai, J., and Hastings, M. G.: Theoretical Phase Resolved Ammonia-Ammonium  
685 Nitrogen Equilibrium Isotope Exchange Fractionations: Applications for Tracking Atmospheric  
686 Ammonia Gas-to-Particle Conversion, *ACS Earth Space Chem.*, 3, 79-89,  
687 10.1021/acsearthspacechem.8b00140, 2019.
- 688 Wang, G., Kawamura, K., Xie, M., Hu, S., Li, J., Zhou, B., Cao, J., and An, Z.: Selected water-soluble  
689 organic compounds found in size-resolved aerosols collected from urban, mountain and marine  
690 atmospheres over East Asia, *Tellus Series B-Chemical and Physical Meteorology*, 63, 371-381,  
691 10.1111/j.1600-0889.2011.00536.x, 2011.
- 692 Wang, G., Zhang, R., Gomez, M. E., Yang, L., Zamora, M. L., Hu, M., Lin, Y., Peng, J., Guo, S., Meng,  
693 J., Li, J., Cheng, C., Hu, T., Ren, Y., Wang, Y., Gao, J., Cao, J., An, Z., Zhou, W., Li, G., Wang, J.,



- 694 Tian, P., Marrero-Ortiz, W., Secretst, J., Du, Z., Zheng, J., Shang, D., Zeng, L., Shao, M., Wang, W.,  
695 Huang, Y., Wang, Y., Zhu, Y., Li, Y., Hu, J., Pan, B., Cai, L., Cheng, Y., Ji, Y., Zhang, F., Rosenfeld,  
696 D., Liss, P. S., Duce, R. A., Kolb, C. E., and Molina, M. J.: Persistent sulfate formation from London  
697 Fog to Chinese haze, *Proc. Natl. Acad. Sci. USA*, 113, 13630-13635, 10.1073/pnas.1616540113,  
698 2016.
- 699 Wang, G. H., Zhou, B. H., Cheng, C. L., Cao, J. J., Li, J. J., Meng, J. J., Tao, J., Zhang, R. J., and Fu, P.  
700 Q.: Impact of Gobi desert dust on aerosol chemistry of Xi'an, inland China during spring 2009:  
701 differences in composition and size distribution between the urban ground surface and the mountain  
702 atmosphere, *Atmos. Chem. Phys.*, 13, 819-835, 10.5194/acp-13-819-2013, 2013.
- 703 Wankel, S. D., Chen, Y., Kendall, C., Post, A. F., and Paytan, A.: Sources of aerosol nitrate to the Gulf of  
704 Aqaba: Evidence from delta N-15 and delta O-18 of nitrate and trace metal chemistry, *Mar. Chem.*,  
705 120, 90-99, 10.1016/j.marchem.2009.01.013, 2010.
- 706 Wexler, A. S. and Seinfeld, J. H.: Second-generation inorganic aerosol model, *Atmos. Environ.*, 25A,  
707 2731-2748, 1991.
- 708 Wu, C., Liu, L., Wang, G., Zhang, S., Li, G., Lv, S., Li, J., Wang, F., Meng, J., and Zeng, Y.: Important  
709 contribution of N<sub>2</sub>O<sub>5</sub> hydrolysis to the daytime nitrate in Xi'an, China during haze periods: Isotopic  
710 analysis and WRF-Chem model simulation, *Environmental pollution (Barking, Essex : 1987)*, 288,  
711 117712-117712, 10.1016/j.envpol.2021.117712, 2021.
- 712 Wu, C., Wang, G., Li, J., Li, J., Cao, C., Ge, S., Xie, Y., Chen, J., Liu, S., Du, W., Zhao, Z., and Cao, F.:  
713 Non-agricultural sources dominate the atmospheric NH<sub>3</sub> in Xi'an, a megacity in the semi-arid region  
714 of China, *Sci. Total Environ.*, 722, 137756, 10.1016/j.scitotenv.2020.137756, 2020a.
- 715 Wu, C., Wang, G., Li, J., Li, J., Cao, C., Ge, S., Xie, Y., Chen, J., Li, X., Xue, G., Wang, X., Zhao, Z.,  
716 and Cao, F.: The characteristics of atmospheric brown carbon in Xi'an, inland China: sources, size  
717 distributions and optical properties, *Atmos. Chem. Phys.*, 20, 2017-2030, 10.5194/acp-20-2017-  
718 2020, 2020b.
- 719 Wu, C., Zhang, S., Wang, G., Lv, S., Li, D., Liu, L., Li, J., Liu, S., Du, W., Meng, J., Qiao, L., Zhou, M.,  
720 Huang, C., and Wang, H.: Efficient Heterogeneous Formation of Ammonium Nitrate on the Saline  
721 Mineral Particle Surface in the Atmosphere of East Asia during Dust Storm Periods, *Environ. Sci.*  
722 *Technol.*, 54, 15622-15630, 10.1021/acs.est.0c04544, 2020c.
- 723 Xie, Y., Wang, G., Wang, X., Chen, J., Chen, Y., Tang, G., Wang, L., Ge, S., Xue, G., Wang, Y., and Gao,  
724 J.: Nitrate-dominated PM<sub>2.5</sub> and elevation of particle pH observed in urban Beijing during the  
725 winter of 2017, *Atmos. Chem. Phys.*, 20, 5019-5033, 10.5194/acp-20-5019-2020, 2020.
- 726 Xu, Z., Huang, X., Nie, W., Shen, Y., Zheng, L., Xie, Y., Wang, T., Ding, K., Liu, L., Zhou, D., Qi, X.,  
727 and Ding, A.: Impact of Biomass Burning and Vertical Mixing of Residual-Layer Aged Plumes on  
728 Ozone in the Yangtze River Delta, China: A Tethered-Balloon Measurement and Modeling Study of  
729 a Multiday Ozone Episode, *J. Geophys. Res.-Atmos.*, 123, 11786-11803, 10.1029/2018jd028994,  
730 2018.
- 731 Yeatman, S. G., Spokes, L. J., Dennis, P. F., and Jickells, T. D.: Can the study of nitrogen isotopic  
732 composition in size-segregated aerosol nitrate and ammonium be used to investigate atmospheric  
733 processing mechanisms?, *Atmos. Environ.*, 35, 1337-1345, 10.1016/s1352-2310(00)00457-x, 2001.
- 734 Yi, Y., Meng, J., Hou, Z., Wang, G., Zhou, R., Li, Z., Li, Y., Chen, M., Liu, X., Li, H., and Yan, L.:  
735 Contrasting compositions and sources of organic aerosol markers in summertime PM(2.5 )from  
736 urban and mountainous regions in the North China Plain, *Sci. Total Environ.*, 766,  
737 10.1016/j.scitotenv.2020.144187, 2021.



738 Zhang, Y., Forrister, H., Liu, J., Dibb, J., Anderson, B., Schwarz, J. P., Perring, A. E., Jimenez, J. L.,  
739 Campuzano-Jost, P., Wang, Y., Nenes, A., and Weber, R. J.: Top-of-atmosphere radiative forcing  
740 affected by brown carbon in the upper troposphere, *Nat. Geosci.*, 10, 486-+, 10.1038/ngeo2960,  
741 2017.

742 Zheng, B., Tong, D., Li, M., Liu, F., Hong, C., Geng, G., Li, H., Li, X., Peng, L., Qi, J., Yan, L., Zhang,  
743 Y., Zhao, H., Zheng, Y., He, K., and Zhang, Q.: Trends in China's anthropogenic emissions since  
744 2010 as the consequence of clean air actions, *Atmos. Chem. Phys.*, 18, 14095-14111, 10.5194/acp-  
745 18-14095-2018, 2018.

746 Zhou, S., Wu, L., Guo, J., Chen, W., Wang, X., Zhao, J., Cheng, Y., Huang, Z., Zhang, J., Sun, Y., Fu, P.,  
747 Jia, S., Tao, J., Chen, Y., and Kuang, J.: Measurement report: Vertical distribution of atmospheric  
748 particulate matter within the urban boundary layer in southern China - size-segregated chemical  
749 composition and secondary formation through cloud processing and heterogeneous reactions,  
750 *Atmos. Chem. Phys.*, 20, 6435-6453, 10.5194/acp-20-6435-2020, 2020.

751  
752  
753  
754  
755  
756  
757  
758  
759  
760  
761  
762  
763  
764  
765  
766  
767  
768  
769  
770  
771  
772  
773  
774  
775  
776  
777  
778  
779  
780  
781



782

783

784

785 **Table caption**

786 Table 1 Mass concentrations of species in the PM<sub>2.5</sub> samples and the meteorological  
787 conditions at the two sampling sites.

788

789

790

791 **Figure captions**

792

793 Figure 1 (a) Location of the study sites in China, (b) topographic view of Mt. Hua  
794 with the sampling sites marked, and (c) vertical views of the two sampling sites and  
795 the horizontal distance between them. (The maps are produced by mapbox,  
796 <https://account.mapbox.com/>, last access, 31 Dec. 2021).

797

798 Figure 2 Time series of the temperature (T), relative humidity (RH), boundary layer  
799 height (BLH) and mass concentrations of PM<sub>2.5</sub> and the water-soluble ions in PM<sub>2.5</sub>  
800 during the observation period at the two sampling sites.

801

802 Figure 3 Diurnal variations in PM<sub>2.5</sub> and the boundary layer height (BLH) at the  
803 different observation sites.

804

805 Figure 4 Concentration-weighted trajectory (CWT) analyses of PM<sub>2.5</sub> in both the  
806 daytime (8:00-20:00) and nighttime (21:00-7:00) at the MS site.

807

808 Figure 5 Mass closure of PM<sub>2.5</sub> during the observed period (OM=1.6×OC).

809

810 Figure 6 Comparison of the calculated and observed NH<sub>4</sub><sup>+</sup> concentrations at the MF  
811 and MS sampling sites.

812

813 Figure 7 Schematic of the physicochemical behaviors of nitrate and ammonium during  
814 the transport process.

815

816 Figure 8 Temperature dependence of the ratio of the product of the partial pressures of  
817 NH<sub>3</sub> and HNO<sub>3</sub> with the dry dissociation constant of NH<sub>4</sub>NO<sub>3</sub>.

818

819 Figure 9 Nitrate and ammonium δ<sup>15</sup>N values at the two sampling sites in the daytime.

820

821

822

823

824

825

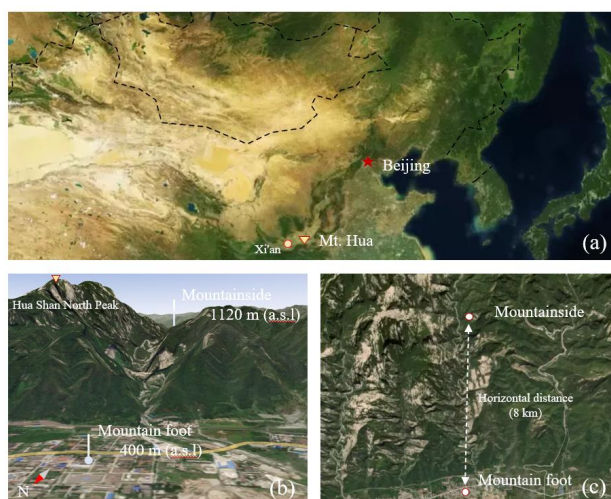


826  
827 Table 1 Mass concentrations of species in the PM<sub>2.5</sub> samples, pH and the  
828 meteorological conditions at the two sampling sites.

	Mountain foot	Mountainside
(i) Mass concentration in species ( $\mu\text{g}/\text{m}^3$ )		
SO <sub>4</sub> <sup>2-</sup>	10.1±6.4	9.0±7.1
NO <sub>3</sub> <sup>-</sup>	6.1±6.3	3.8±5.8
NH <sub>4</sub> <sup>+</sup>	3.9±3.3	3.9±3.5
Cl <sup>-</sup>	0.4±0.5	0.4±0.5
Na <sup>+</sup>	0.7±0.8	1.7±3.1
K <sup>+</sup>	0.2±0.3	0.4±0.4
Mg <sup>2+</sup>	0.1±0.1	0.1±0.1
Ca <sup>2+</sup>	2.5±2.0	0.9±1.2
OC	14.0±4.7	5.0±2.8
EC	4.3±2.0	1.1±0.7
PM <sub>2.5</sub>	76.0±44.1	47.0±38.0
pH <sup>a</sup>	3.4±2.2	2.9±2.0
(ii) Meteorological parameters		
T (°C)	23.2±4.2	15.0±2.5
RH (%)	68.9±18.2	62.8±20.0
Wind speed (m/s)	1.3±1.1	3.2±2.0
Visibility (km)	14.1±9.5	22.2±12.1

<sup>a</sup>pH is predicted by the thermodynamic model (E-AIM (IV))

829  
830

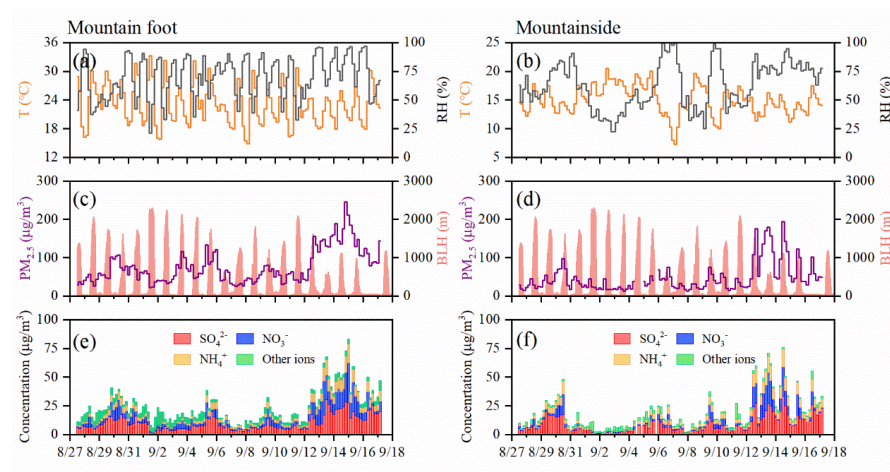


831  
832 Figure 1 (a) Location of the study sites in China, (b) topographic view of Mt. Hua  
833 with the sampling sites marked, and (c) vertical views of the two sampling sites and  
834 the horizontal distance between them. (The maps are produced by mapbox,  
835 <https://account.mapbox.com/>, last access, 31 Dec. 2021).



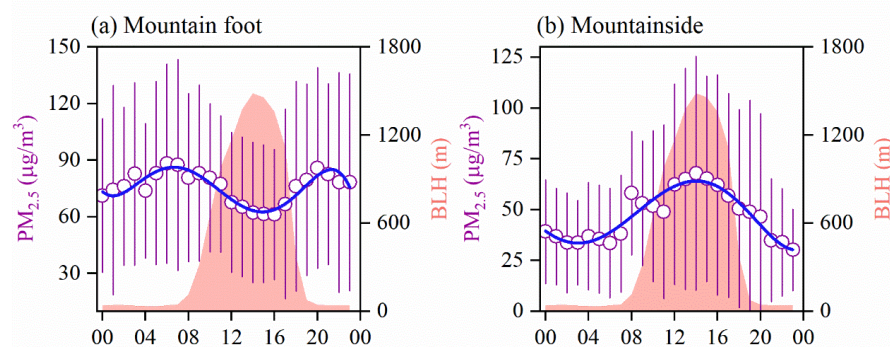


836  
837  
838



839  
840  
841  
842  
843  
844  
845  
846  
847  
848  
849  
850

Figure 2 Time series of the temperature (T), relative humidity (RH), boundary layer height (BLH) and mass concentrations of PM<sub>2.5</sub> and the water-soluble ions in PM<sub>2.5</sub> during the observation period at the two sampling sites.

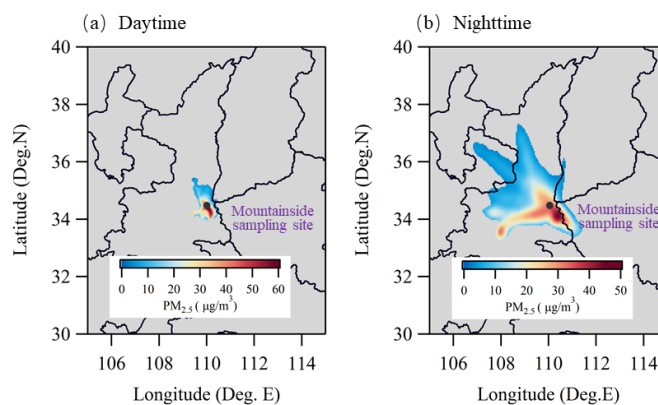


851  
852  
853  
854  
855

Figure 3 Diurnal variations in PM<sub>2.5</sub> and the boundary layer height (BLH) at the two sampling sites.

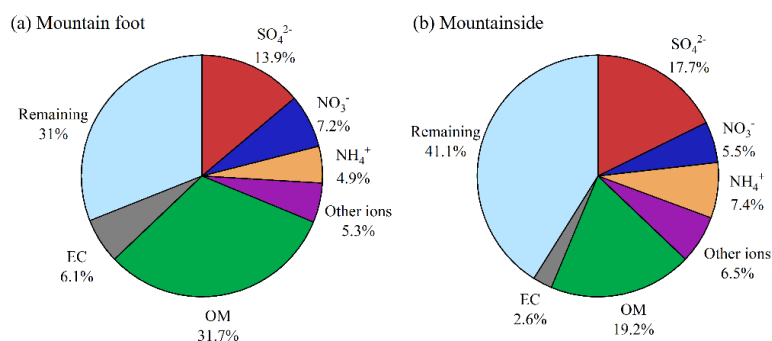


856  
 857  
 858  
 859  
 860



861  
 862 Figure 4 Concentration-weighted trajectory (CWT) analyses of  $PM_{2.5}$  in both the  
 863 daytime (8:00-20:00) and nighttime (21:00-7:00) at the MS site.

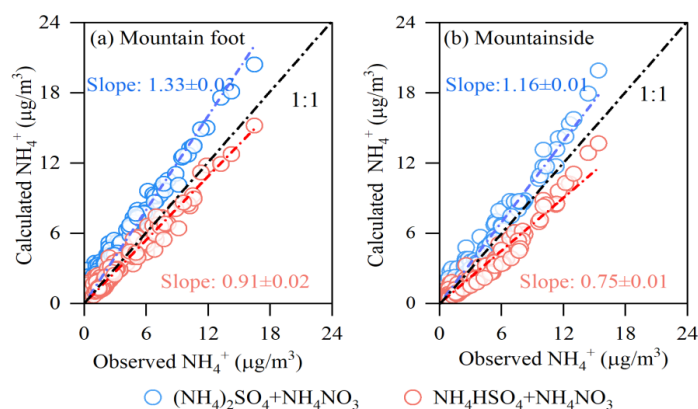
864  
 865  
 866  
 867  
 868  
 869  
 870



871  
 872 Figure 5 Mass closure of  $PM_{2.5}$  during the observed period ( $OM=1.6\times OC$ ).  
 873  
 874  
 875  
 876  
 877

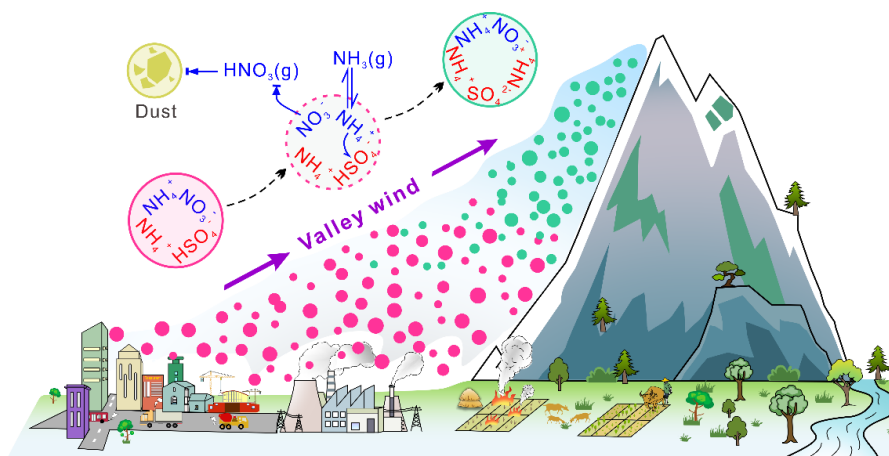


878  
879  
880  
881



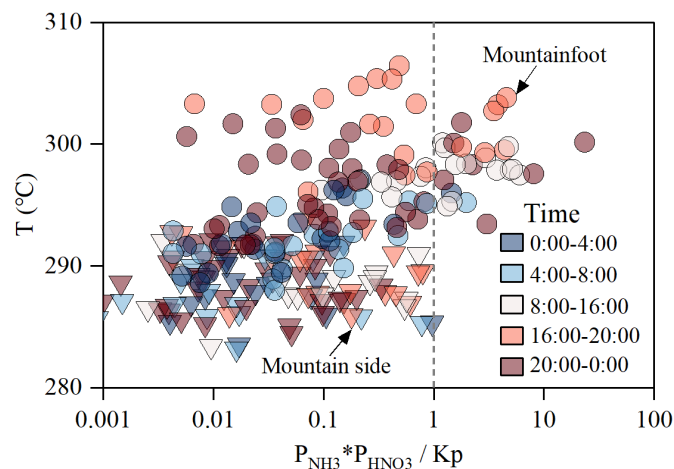
882  
883  
884  
885  
886  
887  
888  
889

Figure 6 Comparison of the calculated and observed  $\text{NH}_4^+$  concentrations at both sampling sites.

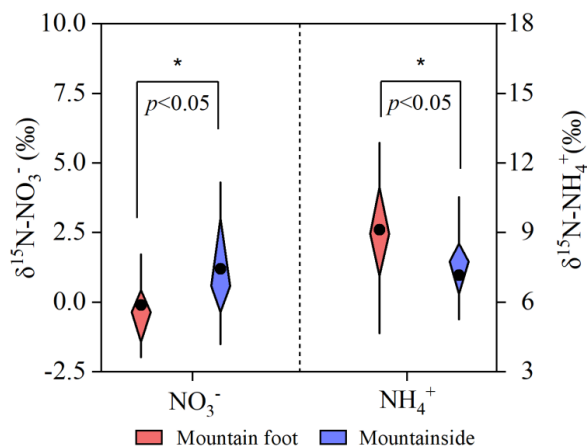


890  
891  
892  
893  
894

Figure 7 Schematic of the physicochemical behaviors of nitrate and ammonium during the transport process.



895  
 896 Figure 8 Temperature dependence of the ratio of the product of the partial pressures of  
 897  $\text{NH}_3$  and  $\text{HNO}_3$  with the dry dissociation constant of  $\text{NH}_4\text{NO}_3$ .  
 898  
 899  
 900  
 901  
 902  
 903



904  
 905 Figure 9 Nitrate and ammonium  $\delta^{15}\text{N}$  values at the two sampling sites in the daytime.  
 906